

A Liquid-Core Fiber Platform for Classical and Entangled Two-Photon Absorption Measurements

Kristen M. Parzuchowski,^{†,‡,¶} Michael D. Mazurek,^{¶,‡} Charles H. Camp Jr.,[§]
Martin J. Stevens,^{||} and Ralph Jimenez^{*,†,⊥}

[†]*JILA, University of Colorado Boulder, Colorado 80309, USA*

[‡]*Department of Physics, University of Colorado Boulder, Colorado 80309, USA*

[¶]*Associate of the National Institute of Standards and Technology, Boulder, Colorado 80305, USA*

[§]*National Institute of Standards and Technology, Gaithersburg, Maryland 20899, USA*

^{||}*National Institute of Standards and Technology, Boulder, Colorado 80305, USA*

[⊥]*Department of Chemistry, University of Colorado Boulder, Colorado 80309, USA*

E-mail: rjimenez@jila.colorado.edu

Abstract

We introduce a toluene-filled fiber platform for two-photon absorption measurements. By confining both the light and molecular sample inside the 5 μm hollow core of the fiber, we increase the distance over which the nonlinear light-matter interaction occurs. With only a 7.3 nL excitation volume, we measure classical two-photon absorption (C2PA) at an average laser power as low as 1.75 nW, which is a 45-fold improvement over a conventional free-space technique. We use this platform to attempt to measure entangled two-photon absorption (E2PA), a process with a limited operating regime due to a crossover in dominating processes from E2PA to C2PA as photon flux is increased. Recently, several teams of researchers have reported that E2PA cross sections are much smaller than previously claimed. As a result, the process dominates at photon fluxes so low that it is extremely difficult or impossible to measure using conventional free-space techniques. In this report, we implement the first E2PA measurement using a waveguide. We see no evidence of E2PA, and we set an up-

per bound on the cross section consistent with these recent reports.

1 Introduction

Liquid-core fibers (LCF) provide platforms for material characterization,¹ optical limiting,² sensing³ and light generation.^{4,5} These fibers are designed using a variety of geometries and materials that aid in their ability to confine light into micrometer-scale cores over centimeter-scale distances. The light reaches high intensities within LCF, which enables nonlinear processes to dominate^{6,7} and thus become easier to observe than in conventional free-space techniques. Processes like four-wave mixing, third-harmonic generation, supercontinuum generation, Raman scattering and two-photon absorption (2PA) have been targeted in LCF.

Two-photon absorption was first observed in capillary LCFs in the 1990s.^{8,9} These studies included models that were used to derive molecular 2PA coefficients from measurements of energy transmitted out of the fiber as a function of energy sent into the fiber.^{10,11} A number of

2PA fiber studies have followed these, including 2PA observed in liquid- or vapor-core photonic crystal fibers^{12,13} and using tapered or exposed-core fiber.^{14,15} One study in particular¹² used a water-filled photonic-crystal-fiber system to measure a 2PA signal at analyte concentrations as low as 10^{-9} M ($M = \text{mol L}^{-1}$), which is roughly four orders-of-magnitude smaller than typical concentrations used in free-space configurations. Although a one-to-one comparison of the two techniques was not performed, this report exemplifies how sensitive LCF techniques can lead to significant improvements in 2PA signal levels.

Here, we show that with a toluene-filled fiber, 2PA cross sections, which are the quantities that describe the strength of the 2PA process, can be measured at extremely low powers. To the best of our knowledge, this work is the first to show a 2PA measurement at an average power as low as 1.75 nW. This is a 45-fold lower power than that achieved in our previous results¹⁶ for low-power 2PA in free space for the same sample. These fiber and free-space measurements serve as a one-to-one comparison since both were designed to test the sensitivity limits of the platforms. We believe this is the first time that the advantage of the fiber platform for 2PA has been quantified.

This sensitivity, paired with the ability to increase our laser power by up to nine orders of magnitude, demonstrates that the platform is well equipped to boost previously undetectable signals. This is necessary, for example, for measurements of C2PA cross sections at much less efficient wavelengths or for much less efficient absorbers. Furthermore, rather than being limited to a high peak power laser,¹⁷ unconventional light sources may produce sizeable 2PA signals.

One such light source is an entangled photon pair source based on spontaneous parametric downconversion (SPDC). We employ an SPDC source in an attempt to measure entangled two-photon absorption (E2PA). To differentiate between E2PA and 2PA excited by a laser source, we refer to the latter process as classical two-photon absorption (C2PA). The E2PA process has been a subject of theoretical study since

the 1980s (Refs. 18–20), driven by the idea that the strong temporal and spatial correlations of SPDC photons are ideal for 2PA. These temporal and spatial correlations are characterized by the entanglement time and area, respectively.²⁰ This absorption process is known to scale linearly with the excitation photon flux, rather than the quadratic scaling of C2PA, at low photon flux where it dominates over C2PA and thus demonstrates a quantum advantage.

Recently, a wide range of evidence from a variety of experimental research studies has shown that molecular E2PA cross sections are much smaller than previously reported. The majority of studies have reported no E2PA signal above the noise floor (Refs. 16,21–30). One study has reported an extremely weak signal (Ref. 31). These experimental reports have been reinforced by recent theoretical works that show that the linear scaling will dominate at photon fluxes so low that the resulting minuscule signal will be difficult or impossible to measure with current technology (Refs. 32–35). Furthermore, the conditions under which the minuscule signal is maximized require careful selection of the SPDC source and two-photon absorber. These experimental and theoretical studies all consider conventional free-space excitation conditions. Here we present, to the best of our knowledge, the first E2PA measurement implemented in a waveguide. We do not observe E2PA and set an upper bound on the E2PA cross section of the molecule AF455.

In this paper, we discuss the principles of our experimental scheme and the design considerations along with our experimental implementation and its characterization. Next, we present our results for excitation of the molecule AF455 with both laser and SPDC photons and derive the C2PA and E2PA cross sections, respectively. Finally we compare our results with those from previous free-space measurements.¹⁶ More details on experimental characterization, data acquisition and data analysis are provided in the supplemental information.

2 Operating Principles

We confine both a sample (two-photon-absorbing molecules in solution) and an excitation beam in the core of a hollow-core fiber. Here the goal is to excite the confined molecules by 2PA. The excited molecules sometimes emit fluorescence and some of that light is guided back out of the fiber and can be detected.

The benefit of this scheme is illustrated in Fig. 1(a-b). In the free-space approach (Fig. 1(a)), light is focused into the cuvette to a waist w_0 and diverges on a length scale characterized by the Rayleigh range z_R which scales quadratically with w_0 . Thus, increasing beam intensity occurs at the cost of maintaining the intensity over a shorter distance z_R . For typical focusing conditions of $w_0 \approx 30 \mu\text{m}$ for an 810 nm beam into toluene, $z_R \approx 5.2 \text{ mm}$, which is about half of the cuvette’s length. In contrast, with the fiber-based approach (Fig. 1(b)), the beam waist w_0 is maintained with low loss over the entire propagation length of the fiber because of optical confinement. Typically, w_0 is much smaller in fiber than in free space. This high light intensity is advantageous for 2PA because two photons must be spatially and temporally overlapped at a molecule for absorption to occur. Maintaining the peak intensity of the focused beam over centimeter length-scales increases the excitation probability because of the interaction with a large number of molecules.

To achieve broadband guidance of both the excitation and fluorescence photons, we selected our fiber for index guidance. In this regime, nearly all light traveling in the core and incident onto the core-cladding interface at an angle (with respect to the normal to the interface) equal to or greater than the critical angle, $\theta_c = \arcsin(n_{\text{clad}}/n_{\text{core}})$ where n_{clad} and n_{core} are the indices of refraction of the cladding and core of the fiber, is guided through the fiber by total internal reflection. It is likely that our cladding material is imperfect, due in part to optical losses and its finite extent, and results in a minor deviation from perfect total internal reflection. The critical angle is only a real number if the refractive index of the cladding is smaller than that of the core. To satisfy this criterion,

we use a standard capillary tubing (inner diameter = $5 \mu\text{m}$, outer diameter = $150 \mu\text{m}$) with a silica cladding and fill the hollow core with toluene. The critical angle under these conditions is real for both the excitation and fluorescence wavelength regions. Many other common solvents, such as water, methanol or chloroform, have indices of refraction smaller than that of silica.

The refractive indices as a function of wavelength for the toluene core and silica cladding are plotted in Fig. 1(c) using the known dispersion equations for the materials.^{36,37} The effective index of refraction of the fundamental and second-order modes are shown and are calculated using Ref. 38. We can estimate the number of modes that can propagate along the fiber, which has a core diameter d , using the V-number,

$$V(\lambda) = \frac{\pi d}{\lambda} \sqrt{n_{\text{core}}^2(\lambda) - n_{\text{clad}}^2(\lambda)}. \quad (1)$$

The number of modes that can propagate at a particular wavelength λ is then $V^2(\lambda)/2$. For the excitation wavelength of 810 nm, approximately 16 modes can propagate in our LCF. For the fluorescence wavelengths of AF455 in toluene, which is peaked at 451 nm, approximately 80 modes can propagate. In the ideal case, all the light would remain in the fundamental mode because this mode experiences the lowest loss, has lower dispersion and has a Gaussian spatial profile. All these characteristics will increase the rate of 2PA.

In addition to toluene allowing broadband guidance of light in a silica fiber, this solvent also has a low absorption coefficient³⁹ at the excitation and fluorescence wavelengths (0.0030 cm^{-1} and 0.0039 cm^{-1} , respectively). This is a necessary condition otherwise the long length of the fiber will add little to no benefit since all the light would be absorbed after a short distance. For comparison, water has an absorption coefficient that is about one order of magnitude larger at 810 nm (0.0209 cm^{-1} ³⁹).

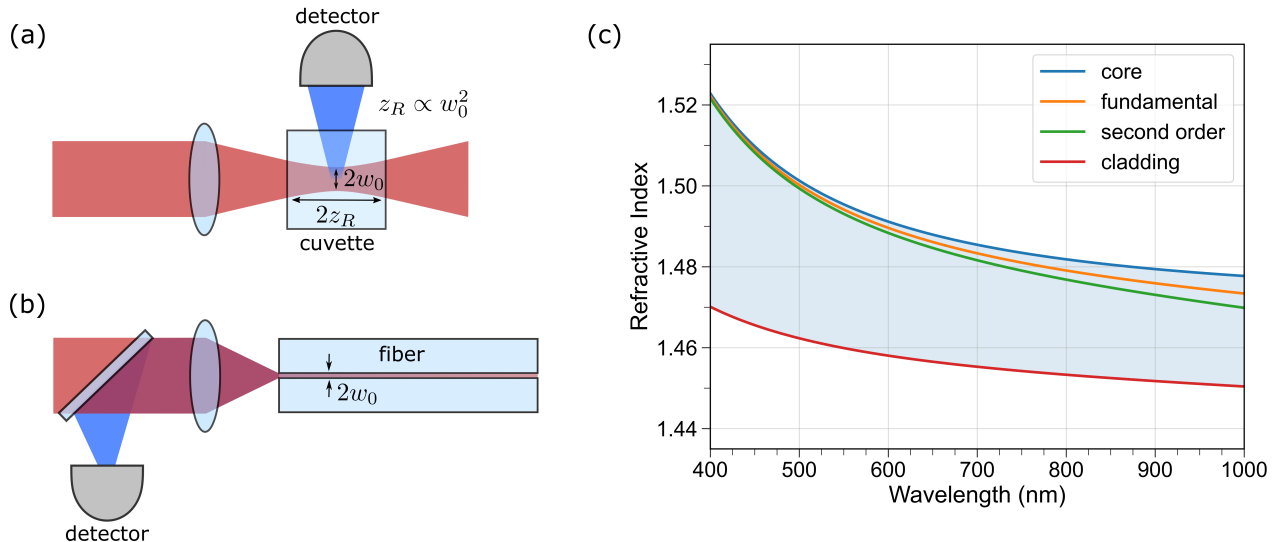


Figure 1: Illustration of (a) a conventional free-space and (b) a fiber-based 2PA measurement scheme. In the free-space approach, the light is focused into the cuvette to a beam waist w_0 . The Rayleigh range z_R characterizes the distance over which the beam size is $\leq \sqrt{2}w_0$. When w_0 is decreased so is z_R , thus high intensity beams can only be maintained over short distances. Fluorescence is generated primarily at the waist of the beam and the fraction emitted in the direction of the detector is collected. In the fiber-based approach, the light is focused into fiber with waist w_0 and maintained over long lengths. Fluorescence is generated along the length of the fiber and the fraction directed opposite of the excitation beam is collected on a detector. (c) Refractive index as a function of wavelength for the relevant media and first two modes of guided light. The toluene-filled core (blue) and silica cladding (red) indices are shown. The mode indices for the fundamental (orange) and second-order (green) modes are shown. Additional modes can propagate through the filled fiber with mode indices filling the blue shaded region between the second-order mode and cladding indices.

3 Materials and Methods

To prepare the fiber, we first cut clean facets on both ends to minimize light-coupling losses. We use a custom-built coil heater to remove about 20 mm of the polyamide coating from each end, then we cleave the fiber ends in the regions where the coatings were removed. We inspect the ends under a digital microscope (Keyence VHX 7000) to ensure the cuts are smooth and to check for particle contamination. Typical images are shown in Fig. 2(a)-(b). The fiber ends are placed in a tubing sleeve to prevent breakage and to allow for simple attachment to the custom-built fiber adapters (similar to those used in Refs. 40,41, technical drawings provided in Ref. 42).

The fiber and tubing sleeves are secured into the fiber adapters as shown in Fig. 3. One fiber

adapter is connected to a syringe placed into a syringe pump that is used to fill the fiber. Both fiber adapters are connected to valves that serve as drainage ports. The fiber adapters are fitted for fused silica optical windows, which are sealed onto the front for coupling light into and out of fiber. These windows also serve as view-ports to check whether fluid has flowed through the fiber.

The optical and microfluidic setup is illustrated in Fig. 3. Here we give a brief overview of the setup. A complete list of the components is given in Ref. 42. A tunable femtosecond pulsed laser operated at 810 nm (110 fs pulses) is used to generate SPDC photons for E2PA measurements and its direct output is used for C2PA measurements. For photon pair generation, the output is first directed through a second harmonic generation unit to produce 405 nm light.

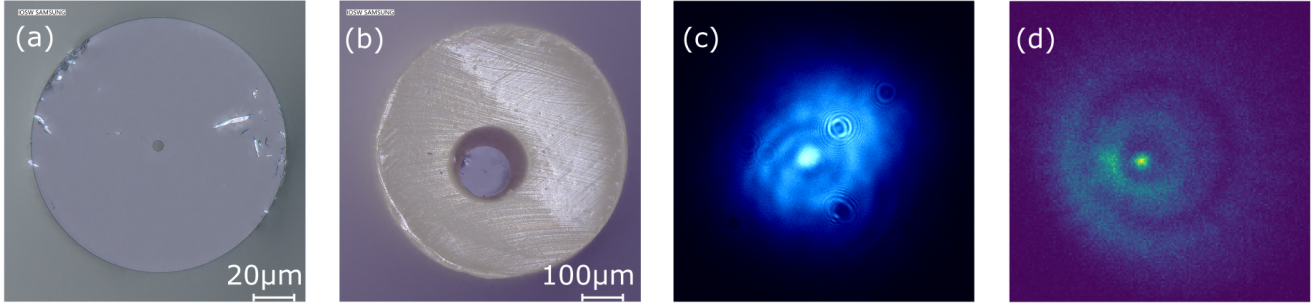


Figure 2: Digital microscope images of one end of (a) the fiber and (b) the fiber inside of the tubing sleeve. (c) sCMOS image of the 810 nm excitation laser guided through the fiber. (d) EMCCD image of the fluorescence from AF455 guided out of the fiber. The last two images are taken in the image plane of the fiber face. Some features of the tube and tubing sleeve are visible in both images as described in Supporting Section 6.

The average power is controlled using a half-wave plate and a polarizer. Spectral filters are used to remove any remaining 810 nm light or unwanted harmonics. A small portion of this beam is picked off by a beam sampler to monitor the power and beam pointing stability of the laser on a quadrant (quad) detector. The blue light is focused ($f = 300$ mm lens) into a 10 mm-long type-0 periodically-poled potassium titanyl phosphate (ppKTP) crystal to generate photon pairs centered at 810 nm. The crystal is temperature controlled at 40.00 ± 0.01 °C. The photon pairs are collimated with a 50 mm lens and any remaining pump light is filtered out.

We measure that this source produces 8.25×10^9 photons s^{-1} mW^{-1} using a scientific Complementary Metal-Oxide-Semiconductor (sCMOS) camera placed directly after the crystal and collimating lens. In our previous report¹⁶ we found that this source has a spectral bandwidth of approximately 75 nm full width at half maximum (FWHM) under these operating conditions. The entanglement time of the SPDC is estimated using a discrete Fourier transform of the joint spectral amplitude, which is estimated using the measured joint spectral intensity (shown in Ref. 16) and a phase estimated using the calculated group delay dispersion accumulated by the SPDC between the center of the crystal and its position along the fiber length. The broadening of the entanglement time across the length of the fiber is taken into

account in our calculations (Supporting Section 10). At the entrance of the fiber the entanglement time is 1070 fs. The entanglement area was not measured, but we estimate it to be in the range of $2.1 \mu m^2$ to $18 \mu m^2$. The lower bound is set by a diffraction limited spot size (see Ref. 16). The upper bound is set by the spot size of the fundamental mode of the fiber.

For the C2PA measurements, the pulsed laser is directed around the nonlinear crystals and through a half-wave plate, polarizing beam-splitter and neutral density filters for control over the power. The light from both sources is recombined at a back-polished mirror. Either source is directed into the fiber-based two-photon excited fluorescence (2PEF) measurement system. First the light propagates through a dichroic beamsplitter and is focused ($f = 10$ mm) into the $5 \mu m$ -diameter-core fiber. Light that is transmitted through the 37 cm-long fiber can be detected on a power meter or imaged on an sCMOS camera as shown in Fig. 2(c). The power before the fiber can be measured with a power meter that flips into the beam path, which doubles as a beam block for background measurements. Any fluorescence generated in the core of the fiber and guided out in the direction opposite of the 810 nm pump beam is reflected at a dichroic beamsplitter and focused onto an Electron-Multiplying Charge-Coupled Device (EMCCD) camera as shown in Fig. 2(d). Spectral filters are used to remove scattered 810 nm light.

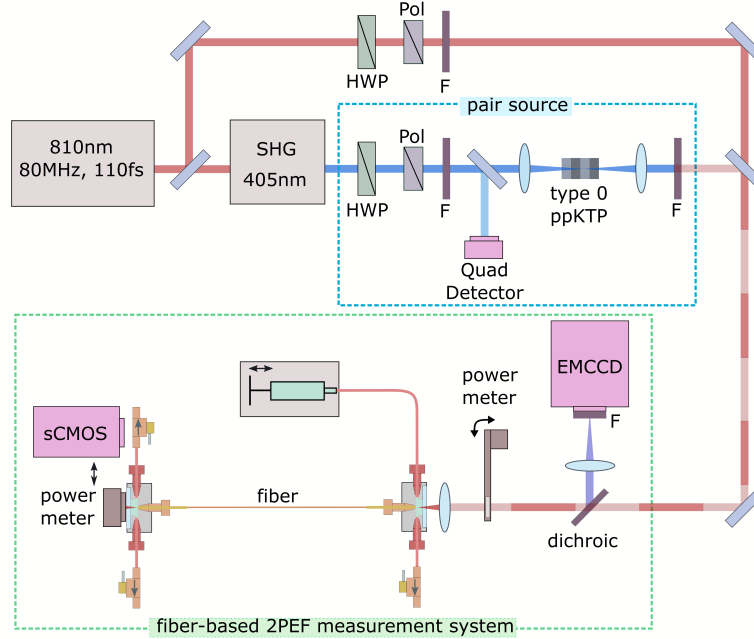


Figure 3: Schematic of the experimental setup. The 810 nm, 110 fs pulsed laser is split. Along one path the light is sent through a second-harmonic generation unit to frequency double the light. It's then sent through a telescope containing a type-0 ppKTP crystal used to generate photon pairs. Along the other path the beam is directed around the nonlinear crystals and is recombined with the light along the other path at a back-polished mirror. Either beam is sent through a dichroic beamsplitter and focused into the fiber held in two fiber adapters at either end. Solvent or a solution is pumped into the fiber using a syringe and syringe pump connected by PEEK tubing to one of the fiber adapters. Light transmitted through the fiber can be detected on a power meter or an sCMOS camera. A fraction of the fluorescence generated in the solution is directed out of the fiber in the direction of the dichroic beamsplitter, where it is reflected and focused onto the EMCCD camera. SHG = second-harmonic generation, HWP = half-wave plate, pol = polarizer, F = spectral filters, 2PEF = two-photon excited fluorescence

Two fibers are used for the experiments: fiber 1 is used for the two lower sample concentration C2PA measurements (experiments 1 and 2) and fiber 2 is used for the highest sample concentration C2PA measurement (experiment 3) and for the E2PA measurement. The summed fiber scattering and toluene absorption coefficients are measured using long exposure images taken by a smartphone camera. The integrated intensity along the length of the fibers is fit to an exponential decay function as shown in Supporting Section 6. The coefficient at 810 nm is determined to be negligible whereas at 458 nm (near the fluorescence maximum) is 0.093 cm^{-1} for fiber 1 and 0.034 cm^{-1} for fiber 2. The measured transmission efficiency of the laser through the fiber was about 40%, 43% and 47%

for experiments 1, 2 and 3 respectively; losses due to coupling, absorption in toluene (11%) and scattering are all accounted for in this efficiency. This high transmission is consistent with the light primarily occupying the fundamental mode. For the SPDC, the transmission efficiency was considerably lower (0.07%). This result is not entirely surprising since the SPDC beam occupies many spatial modes compared to the few-mode fiber. Furthermore, the fiber has a lower retention of light in higher-order modes and thus acts like a single-mode filter. Details on the measurement and definition of transmission efficiency for both laser and SPDC are given in Supporting Section 7.

The sample AF455 is chosen for our measurements due to its large C2PA cross section

at 810 nm and its solubility in toluene. The “AF455” fluorophore is provided by the Air Force Research Laboratory.^{43,44} The toluene used to prepare the sample has a purity of $\geq 99.98\%$. The concentrations were calculated from the one-photon absorption spectra by use of a UV-VIS-NIR spectrophotometer (Agilent Cary 5000 Scan). The concentration of the sample is monitored over the course of a measurement and found to vary by $\leq 12\%$

4 Results and Discussion

Classical two-photon excited fluorescence (C2PEF) datasets were gathered for three different concentrations of AF455 in toluene. Data series were acquired at a variety of laser powers until the uncertainty, set by the Allan deviation, reached a value at least 25% smaller than the photon rate derived from the measurement. For high excitation powers, the acquisition time was as little as five minutes, which produced uncertainty values of less than 1%. Our longest data series was acquired over a 13-hour period, which lowered the uncertainty to the point where the previously indistinguishable signal could be discerned.

An example data series is shown in Fig. 4 for the lowest average excitation power (W_0 in Eq. (4) of the Supporting Information) of 1.75 nW. This data series was acquired over ≈ 13 hours during experiment 3. In Fig. 4(a), the background-subtracted image, which is averaged over the duration of the data series, is shown for the 11x11 superpixel (24x24 pixels per superpixel) region of interest. Near the center of the image a resolved bright spot shows the signal. Without binning this image looks similar to Fig. 2(d).

In Fig. 4(b) the fluorescence rate extracted from each frame’s background-subtracted image is plotted as a function of frame number for both raw (teal) and normalized (pink) data. The normalized data accounts for any changes in laser excitation power (see Supporting Section 8). In Fig. 4(c) the Allan deviation of the fluorescence rate is plotted for different numbers of frames (N) used for averaging for both

raw (teal) and normalized (pink) data. For both Figs. 4(b) and (c), the overlap of the raw and normalized data is indicated by a purple trace. The Allan deviation should follow a $1/\sqrt{N}$ line in the absence of noise sources at that combined frame rate, thus this gold line is used to pick a near optimum number of frames to average. Here, 168 frames is selected, which corresponds to an Allan deviation of 1.3 cnt s^{-1} . We average the data in portions of 168 frames and plot the result in Fig. 4(b) for the raw (gold) and normalized (blue) data. These measurements have an average value of 1.6 cnt s^{-1} .

The results of our fluorescence measurements for three concentrations of AF455 in toluene are plotted in Fig. 5(a), which shows the fluorescence count rate as a function of average excitation power. The fits to the datasets are linear regressions performed on a log-log scale. The slopes of the fits are all within 0.05 of 2.00, which confirms the two-photon origin of the signals. The lowest data point (acquired using the data shown in Fig. 4) is measured for the highest concentration at a power of 1.75 nW. The signals shown here are compared with our model using measured and calculated parameters in Fig. 8 in Supporting Section 10 and show qualitative agreement.

For all three AF455 concentrations, we find that C2PA can be measured at excitation powers significantly lower than is typically possible with a free-space technique. Table 1 compares the parameters used in this experiment to our previous experiment performed in free space.¹⁶ In our previous report, for a sample of 1.10 mM AF455 in toluene, C2PA can be measured down to 79 nW. In this work, we show a 45-fold improvement. The advantage of this platform is ultimately due to the capability to generate high photon fluxes with low average powers by focusing the light to a very small spot size and maintaining it over the length of the fiber. The peak photon flux at our minimum excitation power of 1.75 nW is 1.1×10^{22} photons $\text{cm}^{-2}\text{s}^{-1}$; in the earlier technique at the minimum power of 79 nW, the peak photon flux was 1.3×10^{21} photons $\text{cm}^{-2}\text{s}^{-1}$. Thus, an 8.5-fold higher photon flux was achieved with a 45-fold lower power.

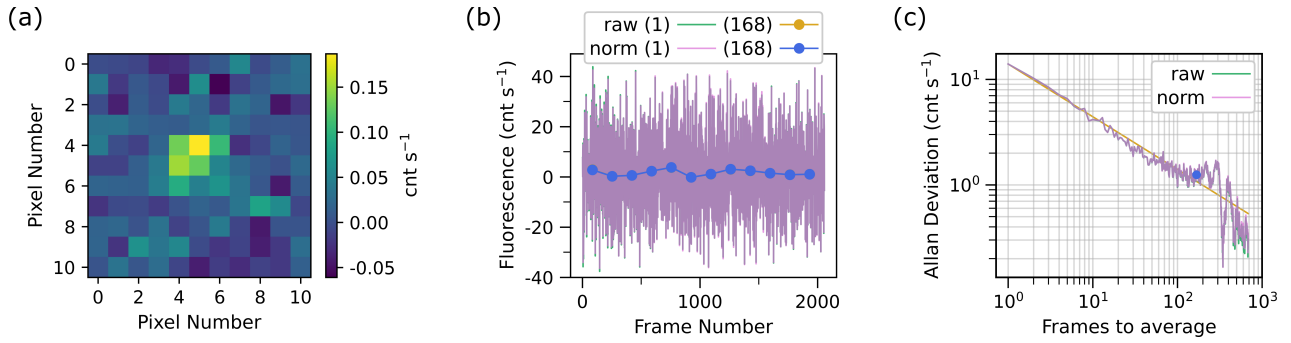


Figure 4: The data series for 1.75 nW average laser excitation power used with the 2.30 mM sample. (a) The average background-subtracted image is shown for the 11x11 superpixel region of interest. (b) The fluorescence rate calculated from each frame’s background-subtracted image is plotted in teal for the raw data or pink for the normalized (norm) data as a function of frame number. The overlap of the raw and normalized data is indicated by the purple trace. Averaging in portions of 168 frames is shown in gold for the raw data or blue for the normalized data. Averaging the normalized data gives a photon rate of 1.6 counts per second (cnt s^{-1}). The normalized data for both the individual and averaged data follows the raw data closely and thus nearly perfectly overlaps the raw data on the plot. This trend indicates a fairly stable laser. (c) The Allan deviation of the photon rate is plotted as a function of number of frames used to average. The teal data shows the Allan deviation of the raw data and the pink shows that for the normalized data. The overlap of the two traces is indicated in purple. A gold $1/\sqrt{N}$ (where N is the number of frames) line is used to guide the eye. The Allan deviation value used in the analysis is indicated by a blue data point, corresponding to averaging portions of 168 frames with an Allan deviation of 1.3 cnt s^{-1} . This data series consists of 2058 frames, which required about 13 hours to collect.

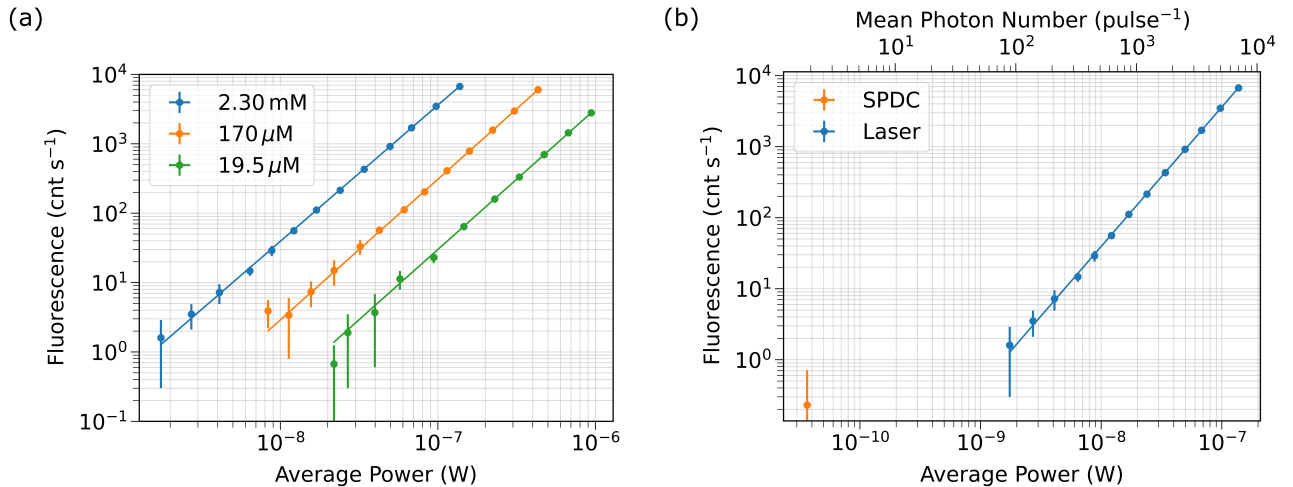


Figure 5: (a) The fluorescence rate measured as a function of the average laser power input to the fiber for a sample of 2.30 mM, $170 \mu\text{M}$ and $19.5 \mu\text{M}$ AF455 in toluene shown in blue, orange and green respectively. The linear fits to the datasets have slopes of 1.96, 2.03 and 2.02 respectively. (b) The fluorescence rate measured as a function of the power input to the fiber for both SPDC (orange) and laser (blue) excitation for a sample of $2.30 \mu\text{M}$ AF455 in toluene. The SPDC measurement is performed at a power 48-fold lower than the minimum laser power and is indistinguishable from zero.

Using Eq. (19) of the Supporting Information, C2PA cross sections are derived using the fits to each of the three concentration datasets. We derive values of (570 ± 190) GM, (340 ± 120) GM and (250 ± 80) GM for the 2.30 mM, 170 μ M and 19.5 μ M samples, respectively. The average of these is (390 ± 80) GM which is in line with the cross sections reported for AF455.^{16,45}

The SPDC source was used exclusively with the 2.30 mM sample. Using the high concentration sample maximizes the likelihood of measuring entangled two-photon excited fluorescence (E2PEF). The results from the SPDC data series are shown in Fig. 6. For this measurement the pump power was nearly maximum for an average of 49.2 mW, which generates 4.06×10^{11} photons s^{-1} . Due to free space losses and fiber coupling losses, only 1.49×10^8 photons s^{-1} make it into the fiber. The average background-subtracted image is shown in Fig. 6(a), where there is no discernible bright spot due to a signal. In Fig. 6(c), the Allan deviation is plotted, which is used to determine a near optimal averaging of 780 frames. This averaging corresponds to an uncertainty of 0.48 cnt s^{-1} for both the raw (teal) and normalized (pink) data. In Fig. 6(b), the fluorescence rate from each frame is plotted as well as the averaged (in 780 frame portions) fluorescence rate. The average fluorescence rate for the raw (gold) data is (0.23 ± 0.48) cnt s^{-1} and for the normalized (blue) data is (0.22 ± 0.48) cnt s^{-1} . The magnitude of the signal is not significantly different from zero, and therefore we conclude that there is no resolvable signal.

Although E2PEF was indistinguishable from zero, there are numerous conclusions to be drawn from these measurements. The C2PEF dataset for the 2.30 mM sample are plotted alongside our E2PEF measurement in Fig. 5(b). Here we show measured fluorescence count rates as a function of the average power of either the SPDC (orange) or laser (blue) source. For the E2PEF measurement, we couple about 36.5 pW of SPDC into the fiber. This plot demonstrates the difference between the SPDC power and the minimum laser power, which are only 48-fold apart.

We can compare these E2PA results with

those done in free space (Table 1). Notably, the power of SPDC at the sample is 60-fold lower in the present experiment. This is due to the difficulties in coupling the SPDC into the few-mode fiber. Despite this lower power, the peak photon flux is 7.7×10^{19} photons $cm^{-2}s^{-1}$. In the free-space studies the SPDC peak photon flux was 2.1×10^{18} photons $cm^{-2}s^{-1}$, which is 37-fold lower. It should be noted that some of the advantage of the higher SPDC photon flux is hindered by the lower fraction of intact photon pairs propagating in the fiber, which is 0.00002% for fiber and 58% for free space. Here we have assumed that the losses are equivalent for both the signal and idler modes that are coupled into fiber. The low pair rate is accounted for in the calculations in Supporting Section 10.

Using Eq. (30) in Supporting Section 10, we set an upper bound on the E2PA cross section of this sample at $(4.0 \pm 1.6) \times 10^{-21}$ cm^2 . This upper bound is for an entanglement time of 1070 fs and an entanglement area in the range 2.1 μm^2 to 18 μm^2 . This entanglement time is an estimated value for the SPDC at the entrance of the fiber adapter. The broadening of the entanglement time in the fiber is among numerous parameters accounted for in the calculation of the upper bound (see Supporting Section 10).

We can compare the upper bound set here to the upper bound set in Ref. 16 for the same sample as shown in Table 1. Since the E2PA cross section is known to scale with parameters of the excitation beam that varied between the two experiments, we cannot compare the two numbers alone. We instead compare the upper bounds using help from the probabilistic model (see for example Ref. 16) and arrive at the ratio R^{UB} ,

$$R^{UB} = \frac{\sigma_E^{UB,1} T_e^1 A_e^1}{\sigma_E^{UB,2} T_e^2 A_e^2}, \quad (2)$$

where T_e and A_e are the entanglement time and area, 1 indicates the current experiment, and 2 indicates the previous experiment.

Although we do not know the exact entanglement areas of the SPDC used in either experiment, the same ppKTP crystal, pump laser and pump focusing conditions were used in both experiments. In the best-case scenario, if the spa-

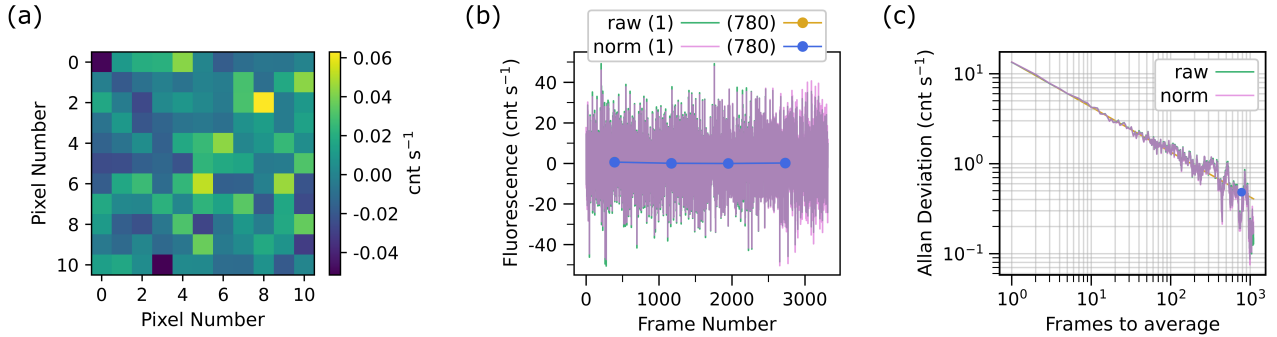


Figure 6: The data series for SPDC excitation of the 2.30 mM sample. (a) The average background-subtracted image is shown for the 11x11 superpixel region of interest. (b) The fluorescence rate calculated from each frame’s background-subtracted image is plotted in teal for the raw data or pink for the normalized (norm) data as a function of frame number. The overlap of the raw and normalized data is indicated by a purple trace. Averaging in portions of 780 frames is shown in gold for the raw data or blue for the normalized data. Averaging the raw and normalized data gives a photon rate of 0.23 cnt s^{-1} and 0.22 cnt s^{-1} respectively. The normalized data for both the individual and averaged data follows the raw data closely and thus nearly perfectly overlaps the raw data on the plot. This trend indicates a fairly stable laser. (c) The Allan deviation of the photon rate is plotted as a function of number of frames used to average. The teal data shows the Allan deviation of the raw data and the pink shows that for the normalized data. A $1/\sqrt{N}$ (where N is the number of frames) line is used to guide the eye and is shown in gold. The Allan deviation value used in the analysis is indicated by a blue data point, corresponding to averaging portions of 780 frames with an Allan deviation of 0.48 cnt s^{-1} for both raw and normalized data. This data series consists of 3316 frames, which required about 24 hours to collect.

tial correlations of the SPDC are maintained as it propagates through the optical system the entanglement area should scale with the beam size at the image plane of the crystal. Since the optical system is designed to image the crystal into the sample, we can use this logic to estimate the ratio of the entanglement areas in the previous experiment to that in the current experiment as the ratio of the respective beam sizes of the SPDC at the sample position. Conveniently, the upper bounds on the entanglement areas are set by these beam sizes. In free space, the E2PA cross section upper bound was set to $(2.1 \pm 0.5) \times 10^{-25} \text{ cm}^2$ for $T_e = 1620 \text{ fs}$ and A_e in the range $2.1 \mu\text{m}^2$ to $13,700 \mu\text{m}^2$. Plugging in the numbers we arrive at R^{UB} of 17. This result indicates that the current experiment sets an upper bound that is 17-fold larger than the previous experiment, and is thus 17-fold less stringent.

5 Conclusions

We presented a toluene-filled fiber platform for two-photon excited fluorescence measurements. We used this platform to measure classical two-photon absorption of various concentrations of the sample AF455. The results of the C2PA measurements show that 2PA can be measured at extremely low powers (1.75 nW) using an excitation volume of only 7.3 nL. This power is 45-fold lower than we achieved previously in free-space under similar conditions (Ref. 16). Furthermore, we derived a classical two-photon absorption cross section for AF455 of $(390 \pm 80) \text{ GM}$. These results emphasize the advantages of liquid-core-fiber platforms for sensing applications where one could instead use higher powers to sense very low concentrations of analytes.

With photon pair excitation, we saw no evidence of a signal, and were ultimately limited by low coupling efficiency of the spatially multi-

Table 1: Comparison of fiber to free-space AF455 measurements.

Parameter	unit	Fiber (this work)	Free space (Ref. 16)
Concentration	mM	2.30	1.10
Min. laser power (flux)	nW ($\text{cm}^{-2}\text{s}^{-1}$)	1.75 (1.1×10^{22}) ^a	79 (1.3×10^{21})
C2PA cross section	GM	390 ± 80	660 ± 180
Entanglement area	μm^2	2.1 to 18	2.1 to 13,700
Entanglement time	fs	1070 ^a	1620
SPDC power (flux)	pW ($\text{cm}^{-2}\text{s}^{-1}$)	36.5 (7.7×10^{19}) ^a	2200 (2.1×10^{18})
SPDC loss	%	99.96 ^a	24
Intact pairs	%	0.00002 ^a	58
E2PA cross section UB R^{UB}	cm^2	$(4.0 \pm 1.6) \times 10^{-21}$	$(2.1 \pm 0.5) \times 10^{-25}$

17

^a This value is valid at the front of the fiber ($z = 0$).

mode SPDC into fiber. Despite this high coupling loss, our calculation of R^{UB} in Section 4, which uses σ_E^{UB} to account for many experimental factors such as loss and the broadening of the entanglement time, shows that the bound we set on the entangled two-photon absorption cross section is 17-fold larger than that set in Ref. 16. Thus, this technique does not provide a higher E2PA sensitivity compared to the free-space technique. However, since the SPDC loss reduces the upper bound in a quadratic manner, efforts to decrease the loss would greatly improve the sensitivity of this technique. This work furthers the growing body of research that has presented null results when attempting to measure entangled two-photon absorption (Refs. 16,21–30,46).

Acknowledgement This work was supported by NIST and by the NSF Physics Frontier Center at JILA (PHY 2317149) and by the NSF-STROBE center (DMR 1548924). We thank S. Mukherjee, A. McLean, H. Greene, K. Thatcher, J. Sipe and C. Drago for valuable suggestions and discussions on the experimental design. We are grateful to T. Loon-Seng Tan and T. Cooper for providing molecular samples. Certain commercial equipment, instruments, or materials are identified in this paper in order to specify the experimental procedure adequately. Such identification is not intended to imply recommendation or endorsement by NIST, nor is it intended to imply that the materials or equip-

ment identified are necessarily the best available for the purpose.

Supporting Information Available

Additional information on experimental characterization, data acquisition and data analysis.

6 Experimental Characterization

In this section we discuss the experimental characterizations we performed to derive C2PA cross sections using Eq. (19) and an E2PA cross section upper bound using Eq. (30). First, we discuss the transmission efficiency of the fiber. Then, we discuss the characterization of propagation losses of the fiber by imaging fiber scatter. Afterwards, we discuss images of the excitation and fluorescence light at the fiber face for qualitative identification of the mode content of the fiber. Finally, we discuss our characterization of the setup’s dispersion.

Before C2PA experiments we maximize the transmission of the 810 nm laser light through the fiber. We measure the power before and after the fiber using power meters, and the ratio of the power transmitted out W_{out} (W) to the power sent in W_{in} (W) is what we call our

transmission efficiency,

$$\begin{aligned}\eta_T &= \frac{W_{\text{out}}}{W_{\text{in}}} \\ &= \eta_C \eta_A(\lambda = \lambda_e, z = l) \eta_S(\lambda = \lambda_e, z = l).\end{aligned}\quad (3)$$

This efficiency is a product of coupling (η_C), absorption (η_A) and scattering (η_S) efficiencies. The latter two efficiencies are evaluated at the excitation wavelength ($\lambda_e = 810$ nm) and for the entire length of the fiber l (cm). The best alignment resulted in $\eta_T > 55\%$. However, during our measurements $\eta_T \approx 43\%$ but varied from data series to data series. We followed the same procedure to measure SPDC transmission efficiency, however we use an sCMOS camera instead of a power meter to measure the incident and output photon count rate. The highest value achieved was $\eta_T \approx 0.058\%$.

We characterize the loss of light along the length z of the fiber by imaging the scattering. The intensity of the scattering is proportional to the power $W(z)$, and thus should exponentially decay according to

$$\begin{aligned}W(z) &= W_0 \times \\ \text{Exp}(-&(a_{\text{sol}}(\lambda) + \epsilon_{\text{sam}}(\lambda)c + \mu(\lambda))z),\end{aligned}\quad (4)$$

where W_0 (W) is the average power at $z = 0$, λ (nm) is the wavelength of the light, $a_{\text{sol}}(\lambda)$ (cm^{-1}) is the absorption coefficient of the solvent, $\epsilon_{\text{sam}}(\lambda)$ ($\text{M}^{-1} \text{cm}^{-1}$) is the extinction coefficient of the sample, c (M) is the concentration of the sample and $\mu(\lambda)$ (cm^{-1}) is the scattering coefficient of the fiber. The parameter W_0 is related to the power measured before the fiber W_{in} (W) by $W_0 = \eta_C W_{\text{in}}$. The power measured at the output of the fiber W_{out} is a good estimate for $W(l)$. The exponential terms related to absorption of the light are $\eta_A(\lambda, z)$ and to scattering of the light is $\eta_S(\lambda, z)$, thus we can rewrite Eq. (4) as

$$W(z) = W_{\text{in}} \eta_C \eta_A(\lambda, z) \eta_S(\lambda, z).\quad (5)$$

With only the solvent in the fiber ($c = 0$), we send a 458 nm (near the peak of our sample's emission spectrum) alignment laser through the fiber and image the scattering on a smart phone camera using long exposure settings as shown in

Fig. 7. The image is integrated along the width of the fiber (vertically) to find an integrated intensity as a function of fiber length. The intensity is fit to the exponential in Eq. (4) to derive $a_{\text{sol}}(458 \text{ nm}) + \mu(458 \text{ nm}) = 0.093 \text{ cm}^{-1}$ for fiber 1 (Fig. 7(a)) and $a_{\text{sol}}(458 \text{ nm}) + \mu(458 \text{ nm}) = 0.034 \text{ cm}^{-1}$ for fiber 2 (Fig. 7(b)). For 458 nm fluorescence, traveling the entire length of the fiber corresponds to a loss of 96.8% or 70.6% of the light for fibers 1 and 2 respectively. We take the same measurement with 750 nm (a visible wavelength close to our excitation wavelength) light and observe no evidence of decay of the scatter along the length of the fiber. We estimate that $a_{\text{sol}}(750 \text{ nm}) + \mu(750 \text{ nm})$ is not large enough to measure this way. As mentioned in Section 2, the values of $a_{\text{sol}}(\lambda)$ are known. From literature,³⁹ $a_{\text{sol}}(750 \text{ nm}) = 0.0036 \text{ cm}^{-1}$ and $a_{\text{sol}}(810 \text{ nm}) = 0.0030 \text{ cm}^{-1}$. If we set $\mu(750 \text{ nm}) = \mu(810 \text{ nm}) = 0$, we find that these absorption coefficients correspond to a loss of 12.5% and 10.5%, respectively, of the light along the length of the fiber. Considering with our best alignment $\eta_T > 55\%$, and that some fraction of that light is lost due to the coupling efficiency in addition to the 10.5% absorption loss, we estimate $\mu(810 \text{ nm}) \approx 0$. This low scattering loss is consistent with the light primarily occupying the fundamental mode of the fiber. From here we can derive that for $\eta_T = 43\%$, $\eta_C = 48\%$.

For SPDC, we are not able to measure η_S due to the low photon rate, and thus cannot quantify the division of losses between η_C and η_S . However, we can consider that η_S will likely only differ from that for laser light if the mode content in the fiber is different. If the SPDC does occupy more higher-order modes than laser light, the higher-order modes tend to have high η_S . This would cause a quick depletion of the modes from the fiber leading to minimal contributions to an E2PA signal. Furthermore, higher-order modes have spatial profiles that are less ideal for 2PA. Thus without losing the bulk of the proper physical model, we will group the scattering losses of the higher-order modes into the coupling loss. Then we can use the same η_S as that determined for the fundamental mode measured with laser light,

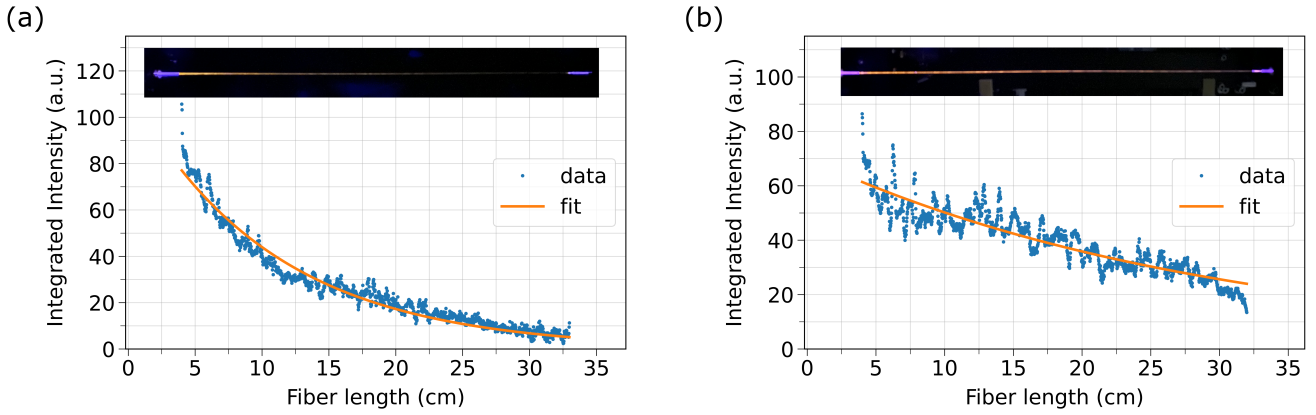


Figure 7: Images of the scatter from the alignment laser (inset) with corresponding plots of the integrated intensity (blue) of the scatter as a function of fiber length for (a) fiber 1 and (b) fiber 2. The intensity of the scatter is higher at the ends due to secondary reflections off the fiber tubing sleeves and fittings. These regions are removed from the plotted data. The fiber is not visible inside of the fittings and fiber adapters. The integrated intensity is fit (orange) to an exponential decay.

and the coupling efficiency will serve as an effective fundamental mode coupling efficiency ($\mu(810\text{ nm}) \approx 0$, $\eta_C = 0.065\%$). We assume that the losses are equivalent for both the signal and idler modes that are coupled into fiber.

We image the 810 nm laser light at the output of the fiber using two lenses before the sCMOS camera, as shown in Fig. 2(c). In this image, the bright larger and smaller concentric circles are the imaged fiber cladding outer diameter and the outline of the core modes, respectively. The larger offset circular shape is likely formed by light guided through the inside of the tubing sleeve as can be seen by comparison to the digital microscope image in Fig. 2(b). Thus, we find that the light occupies some lower intensity cladding and tubing sleeve modes in addition to the dominant core modes.

The fluorescence is collected at the front of the fiber using the lens optimized to focus 810 nm light into the fiber, which roughly collimates the visible fluorescence. The light is reflected at the dichroic beamsplitter, and another lens focuses the image of the fiber face onto the EMCCD, as shown in Fig. 2(d). In this image, the high intensity bright spot is from fluorescence guided through the core. Surrounding that spot is darkness likely from the cladding of the fiber, indicating that there is little light propagating through the cladding of the fiber. Radially outward from the cladding,

light forms an offset circular shape and is likely from light guided through the core of the tubing sleeve as can be seen by comparison to the digital microscope image in Fig. 2(b). A larger circular ring of light surrounds that core, and is likely from light guided through the “cladding” of the tubing sleeve. Thus, the spatial mode content of the fluorescence in the fiber is more complex than the simple calculation in Section 2 assumes, however the highest intensity mode appears to be the fundamental mode of the fiber.

To measure the free-space group delay dispersion (GDD), D_0 (fs²), accumulated by the laser pulse as it propagates through the optical setup, we use the GDD tuning function of the laser. We increase the dispersion compensation in increments of 500 fs² and take C2PA measurements at each step. The step with the maximum C2PA signal corresponds to the value at which the GDD is optimally compensated at the input of the fiber. We measure $D_0 \approx 2000$ fs², $D_0 \approx 2000$ fs² and $D_0 \approx 4000$ fs² for experiments 1, 2 and 3 respectively. For experiments 2 and 3 the free-space dispersion is compensated for using the internal tuning of the laser system. To estimate D_0 accumulated by the SPDC as it propagates through the optical setup, we calculate the GDD of each optical element in its path from the center of the crystal to the entrance of the fiber. We esti-

mate $D_0 \approx 2100 \text{ fs}^2$. To determine the fiber group velocity dispersion (GVD) β ($\text{fs}^2 \text{ cm}^{-1}$), a COMSOL simulation is used to model the filled fiber. The low-order modes are solved for. For the fundamental mode, β is identical to β of toluene, thus there are no contributions from waveguide dispersion. However, for higher-order modes it is likely that β is affected by waveguide dispersion. These higher-order modes are not considered in the calculations of Section 9 or Section 10, and β of the fundamental mode is used.

7 Data Acquisition

In the section we discuss the camera settings used for data acquisition, the characterization of camera baseline and dark count rates, the operations that go into measuring a single frame of data and the conversion of a camera signal to a detected fluorescence rate.

To determine the optimal camera settings, we wrote a script to calculate the expected signal to noise ratio (SNR) of our measurements at various EMCCD settings based on our expected signal levels. We determined the optimum camera settings to be: electron multiplying (EM) output amplifier, EM gain set to 30, preamplifier set to 1, 1 MHz horizontal shift rate, 10 s integration time and 24x24 pixels binned into a superpixel. Although the integration time could be increased further to increase the SNR, we found that clock-induced charge (CIC) occurred more frequently at those integration times. Any obvious CIC was removed from the data, which resulted in a removal of about 6.8% of the frames. To speed up frame readout on the EMCCD, a pixel region of interest (ROI) is selected and only those pixels are read out. To select an ROI, the fluorescence was imaged at a relatively high excitation power and the region with significant photon counts was selected.

Before data series are acquired, the baseline and dark count rates of the camera are characterized. Both are characterized with the built-in camera shutter closed. The baseline data series are taken at the minimum integration time

of the camera. The dark rate data series are taken at the 10 s integration time used for all 2PA data series. From each of these characterization data series we calculate an average value and uncertainty using an Allan deviation analysis like that shown in Fig. 4 for the fluorescence rate. An example baseline average in our ROI yields 560.4 ± 1.3 Analog to Digital Units per pixel (ADU pixel^{-1}) and an example dark rate average in our ROI yields 2.66 ± 0.06 electrons $\text{s}^{-1} \text{ pixel}^{-1}$.

Each two-photon excited fluorescence (2PEF) data frame consists of a background and a signal measurement. The low profile power sensor (Thorlabs S130c) (Fig. 3) is flipped into the beam path to block the beam during a background measurement. For the signal measurement, the power sensor is removed from the beam. We ensured that the power sensor position did not affect the background signal with the laser on. The power sensor after the fiber is used to measure the laser power (W_{out}) before each signal frame and is used to determine W_0 for plotting the power dependence of the signal (Fig. 5(a)). For SPDC data frames, the sCMOS camera is placed at the output of the fiber and used to measure the SPDC power (W_{out}) before each signal frame. The number of data frames acquired at each power varied. As the power decreased, the signal decreased and thus we acquired data for longer to lower the uncertainty.

To calculate the fluorescence rate F in cnt s^{-1} detected by the camera, the pixels of interest are integrated over to determine the camera signal N (ADU). We converted N to a count rate using,

$$F = \frac{NS}{GT}, \quad (6)$$

where S (electrons ADU^{-1}) is the CCD sensitivity for the selected output amplifier and preamplifier, G (electrons cnt^{-1}) is the EM gain and T (s) is the integration time.

8 Data normalization

In this section we discuss the data normalization used to account for fluctuations in excitation power. For this we made use of W_{out} ,

which is measured for each frame, since it accounts for potential changes in η_C due to laser pointing drifts unlike W_{in} .

For laser excitation, each frame's fluorescence rate $F_{i,\text{raw}}$ (cnt s⁻¹) was adjusted to a normalized fluorescence rate for frame i , $F_{i,\text{norm}}$ (cnt s⁻¹), using

$$F_{i,\text{norm}} = F_{i,\text{raw}} \frac{W_{\text{out,avg}}^2}{W_{\text{out},i}^2}, \quad (7)$$

where $W_{\text{out},i}$ (W) is the power transmitted out of the fiber for frame i and $W_{\text{out,avg}}$ (W) is the average power transmitted out of the fiber for the entire data series. Here the normalization uses a quadratic power dependence in accordance with the power scaling of C2PA.

For SPDC excitation, each frame's fluorescence rate $F_{i,\text{raw}}$ was adjusted to a normalized fluorescence rate for frame i using

$$F_{i,\text{norm}} = F_{i,\text{raw}} \frac{W_{\text{out,avg}}}{W_{\text{out},i}}. \quad (8)$$

Here the normalization uses a linear power dependence in accordance with the expected power scaling of E2PA at sufficiently low power.

For all data series, the normalization has minimal effect and alters the value of the data points by less (typically much less) than one Allan deviation. This indicates that the laser is fairly stable throughout each measurement. The normalization is still used to demonstrate that a high level of characterization and analysis is essential, especially for the SPDC measurement.

For the SPDC measurement, a quadrant detector is used to monitor the pump power while the sCMOS camera is used to measure W_{out} . The output power varied over a range of 24% of the maximum value, and decreased monotonically relative to the pump power by 24% over the course of the 24 hour measurement. The latter value is directly related to the decrease in coupling efficiency. The value $\eta_C = 0.065\%$ is the average coupling efficiency.

9 Calculating a C2PA Cross Section

In this section we discuss the assumptions and equations used to calculate a C2PEF signal. We arrive at an equation to derive a C2PA cross section. Finally, we use these equations to model the concentration dependence of the signal and compare with our results.

In a similar manner to that shown in Ref. 16, we can model the C2PEF signal detected on the camera, F_C (cnt s⁻¹), as

$$F_C = g \int_0^l N_C(z) \int_{\lambda_1}^{\lambda_2} \gamma(z, \lambda) \kappa(\lambda) \Phi(\lambda) d\lambda dz, \quad (9)$$

where g (pulses s⁻¹) is the pulse repetition rate, l (cm) is the length of the fiber, $N_C(z)$ (excitations cm⁻¹ pulse⁻¹) is the number of excitations per infinitesimal length of fiber dz (cm) per pulse, λ_1 and λ_2 (nm) are wavelengths chosen such that the integral extends over the entire emission spectrum of the sample, $\gamma(z, \lambda)$ (cnt photon⁻¹) is the component transmission efficiency, $\kappa(\lambda)$ is the geometrical collection efficiency and $\Phi(\lambda)$ (photon excitation⁻¹ nm⁻¹) is the differential fluorescence quantum yield. A proper normalization of quantum yield is used such that $\Phi = \int_0^\infty \Phi(\lambda) d\lambda$ gives the value published in literature for the total quantum yield of the fluorophore.

From Eq. (9), we find that it is advantageous to increase the length of the fiber for all z such that $N_C(z)\gamma(z, \lambda) > 0$. This product never drops below zero, but can be zero if the photons are dispersed in time far enough that two photons are never temporally overlapped at that position z , or if the photon loss along the length l is 100% for either the excitation photons or the fluorescence photons, or some combination of both leading to a negligible product $N_C(z)\gamma(z, \lambda) \approx 0$. Since extra fiber length does not decrease the C2PEF signal, we try to make l long enough that $N_C(l)\gamma(l, \lambda) \approx 0$ so that we can achieve the highest signal at a given photon flux.

Here we define $\kappa(\lambda)$ as the fraction of fluorescence that can be collected by the fiber and

directed out in the direction of the detector. We assume that the fluorescence is emitted isotropically and that the fraction of that light collected can be described by the solid angle of a cone with apex angle $2(90^\circ - \theta_c)$, where θ_c is the critical angle (Section 2). Then we can write,

$$\kappa(\lambda) = \frac{1}{2} \times \left[1 - \cos \left(\sin^{-1} \left(\frac{\sqrt{n_{\text{core}}^2(\lambda) - n_{\text{clad}}^2(\lambda)}}{n_{\text{core}}(\lambda)} \right) \right) \right], \quad (10)$$

where $n_{\text{core}}(\lambda)$ and $n_{\text{clad}}(\lambda)$ are the indices of refraction of the core and cladding materials (toluene and silica) at the wavelength of the fluorescence (peak wavelength $\lambda_f = 451$ nm).

The component transmission efficiency describes the transmission efficiency of fluorescence from its point of generation z (cm) to the detector, under the assumption that it is directed out of the fiber. It takes into account all the loss mechanisms from various optical components and the media the light propagates through. We define this quantity as

$$\begin{aligned} \gamma(z, \lambda) &= \eta_A(\lambda, z) \eta_S(\lambda, z) \mathcal{T}_w(\lambda) \mathcal{T}_{l_1}(\lambda) \times \\ &\quad \mathcal{R}_d(\lambda) \mathcal{T}_{l_2}(\lambda) \mathcal{T}_{f_1}(\lambda) \mathcal{T}_{f_2}(\lambda) \text{QE}(\lambda) \\ &= \eta_A(\lambda, z) \eta_S(\lambda, z) \gamma_0(\lambda), \end{aligned} \quad (11)$$

where $\eta_A(\lambda, z)$ and $\eta_S(\lambda, z)$ are the absorption and scattering efficiencies in fiber (Section 6), $\mathcal{T}(\lambda)$ and $\mathcal{R}(\lambda)$ are the transmittance and reflectance of an optic (w = window, l = lens, d = dichroic beamsplitter and f = spectral filter), and $\text{QE}(\lambda)$ (cnt photon⁻¹) is the quantum efficiency of the camera.

We describe the number of excitations per infinitesimal length dz per pulse as

$$N_C(z) = \frac{1}{2} \sigma_C n \times \int_{-1/2g}^{1/2g} \int_{-\infty}^{\infty} \int_{-\infty}^{\infty} \phi(x, y, z, t)^2 dx dy dt, \quad (12)$$

where σ_C (1 GM = 10^{-50} cm⁴ s photon⁻¹ fluorophore⁻¹) is the C2PA cross section, n (fluorophores cm⁻³) is the number density of the fluorophores and $\phi(x, y, z, t)$ (photons cm⁻² s⁻¹) is the photon flux of the laser beam. The factor of 1/2 carries units of excita-

tions per photons absorbed. The temporal and transverse spatial profiles of the laser beam are approximated by Gaussian distributions. The transverse spatial profile of the light inside the fiber will differ from a Gaussian distribution if the light occupies the higher-order modes of the fiber, but in this calculation we make a few approximations based on the assumption that all the light is in the fundamental mode (Section 6). Assuming the laser is always on, $\phi(x, y, z, t)$ takes the form

$$\begin{aligned} \phi(x, y, z, t) &= \phi_0(z) \text{Exp} \left(-4 \ln 2 \left(\frac{x^2 + y^2}{d_0^2} \right) \right) \\ &\times \sum_{i=-\infty}^{\infty} \text{Exp} \left(-4 \ln 2 \frac{(t + i/g)^2}{\tau(z)^2} \right), \end{aligned} \quad (13)$$

where $\phi_0(z)$ (photons cm⁻² s⁻¹) is the peak photon flux as a function of z , $\tau(z)$ (fs) is the FWHM pulse duration and d_0 (cm) is the FWHM beam width. We use COMSOL to solve for d_0 by first solving for the effective mode area A_{eff} (cm²) of the fundamental mode⁴⁷ and solving

$$d_0 = \sqrt{\frac{2 \ln 2 A_{\text{eff}}}{\pi}}. \quad (14)$$

We can define the average photon rate $Q(z)$ (photons s⁻¹) in terms of the photon flux,

$$\begin{aligned} Q(z) &= g \int_{-1/2g}^{1/2g} \int_{-\infty}^{\infty} \int_{-\infty}^{\infty} \phi(x, y, z, t) dx dy dt \\ &= \frac{W(z)}{h\nu}, \end{aligned} \quad (15)$$

where $W(z)$ (W) is the average power of the beam as a function of z and $h\nu$ (J) is the average energy of an incident photon. We can also write the power in a form to show its dependence on propagation losses in fiber as described in Eq. (4), which brings about its z -dependence.

We can solve for $\phi_0(z)$ by inputting Eq. (13) into Eq. (15) and integrating over x , y and t ,

$$\phi_0(z) = \left(\frac{4 \ln(2)}{\pi} \right)^{3/2} \frac{W(z)}{h\nu g d_0^2 \tau(z)}. \quad (16)$$

The pulse duration has z dependence because

of dispersion and can be described by

$$\tau(z) = \sqrt{\tau_0^4 + (4\ln 2)^2(D_0 + \beta z)^2}/\tau_0, \quad (17)$$

where D_0 (fs²) is the GDD accumulated by the pulse before the fiber and β (fs² cm⁻¹) is the total GVD accumulated by the light in the fundamental mode of the fiber.

Now we can rewrite Eq. (9) using these equations as

$$F_C = \sqrt{2} \left(\frac{\ln(2)}{\pi} \right)^{3/2} \frac{\sigma_C n W_0^2}{g(h\nu)^2 d_0^2} \times \int_0^l \frac{\eta_A^2(\lambda_e, z) \eta_S^2(\lambda_e, z)}{\tau(z)} \int_{\lambda_1}^{\lambda_2} \gamma(z, \lambda) \kappa(\lambda) \Phi(\lambda) d\lambda dz. \quad (18)$$

where $\lambda_e = 810$ nm.

Then we can solve for the C2PA cross section,

$$\sigma_C = \frac{1}{\sqrt{2}} \left(\frac{\pi}{\ln(2)} \right)^{3/2} \frac{g(h\nu)^2 d_0^2}{n} \frac{F_C}{W_0^2} \times \left(\int_0^l \eta_A^2(\lambda_e, z) \eta_S^2(\lambda_e, z) / \tau(z) \times \int_{\lambda_1}^{\lambda_2} \gamma(z, \lambda) \kappa(\lambda) \Phi(\lambda) d\lambda dz \right)^{-1}. \quad (19)$$

All the parameters in Eq. (19) are known through experiments or simulations. The parameters d_0 and β are estimated using COM-

Table 2: Summary of fixed parameters.

Parameter	unit	Laser	SPDC
g	pulses s ⁻¹	8×10^7	
$h\nu$	J	2.45×10^{-19}	
d_0	μm	2.42	
$a_{\text{sol}}(\lambda_e)^a$	cm ⁻¹		0.003
τ_0	fs	110	N/A
β	fs ² cm ⁻¹		1034
$\epsilon(\lambda_f)^a$	M ⁻¹ cm ⁻¹		4417
$\kappa(\lambda_f)^a$			0.0146
Φ	phot excit ⁻¹		0.67 [44]
F^{LB}	cnt s ⁻¹		1.00
\mathcal{T}		N/A	0.565
$T_{e,0}$	fs	N/A	260
S_0		N/A	2145
$Q(0)$	photons s ⁻¹	N/A	1.49×10^8

^a $\lambda_e = 810$ nm, $\lambda_f = 451$ nm

SOL Multiphysics Simulation software, F_C/W_0^2 (cnt s⁻¹ μW^{-2}) is the fit to our experimental C2PEF data (and W_0 is estimated using measured $W(l)$), n is measured using a spectrophotometer, $a_{\text{sol}}(\lambda)$ is from literature,³⁹ $\mu(\lambda)$ is determined from scattering measurements (Section 6), τ_0 is measured using a SwampOptics Grenouille 8-50-USB, D_0 is measured, $k(\lambda)$ is calculated, $\Phi(\lambda)$ is known from published AF455 measurements^{44,45} and $\gamma(z, \lambda)$ is calculated based on optics' specifications, our scattering measurements and the published extinction coefficient and spectra of AF455.⁴⁵ Table 2 and Table 3 summarize parameter values used in this calculation and that described in Section 10.

The uncertainty on derived C2PA cross sections was determined by propagating the errors of the various parameters that go into Eq. (19). We multiply this value by a coverage factor ($k = 2$) to reach $\approx 95\%$ confidence that the true value lies within the bounds set by the error bars. The uncertainty from each experiment is 34%.

In Figure 8, we plot concentration normalized C2PEF ($\frac{F_C}{c}$) at 100 nW from measurements (fit) and calculations (calc) for the experimental conditions of experiments 1 (blue), 2 (orange) and 3 (green). The calculations use Eq. (18) with the values of parameters input from Tables 2 and 3. The uncertainty on these values is propagated, and multiplied by a coverage factor ($k = 2$) to give a total uncertainty of 38% on the calculation (shown by shaded regions). After each experiment, small improvements to the setup were made that resulted in a shift of the curve upwards on the plot as experiments progressed from 1 to 3. The trend of each curve shows the same decrease of $\frac{F_C}{c}$ as a function of c . This general decrease is due to fluorescence re-absorption by the abundant molecules available at high concentrations. The data points from measurements are extracted using quadratic fits (slope fixed to 2.00) to each experiments' data of fluorescence as a function of power. The fit is extrapolated to 100 nW and that value is divided by the measured concentration of the experiment's sample. These data points are within the expected range based on the calcu-

Table 3: Summary of variable parameters. Experiments 1 and 2 (Exp 1 and 2) use the same fiber (fiber 1) and laser excitation. Experiment 3 (Exp 3), which involves both laser and SPDC excitation, uses another fiber (fiber 2).

Parameter	unit	Exp 1	Exp 2	Exp 3	
				Laser	SPDC
F_C/W_0^2	cnt s ⁻¹ μW ²	3.14×10^3	3.19×10^4	3.62×10^5	N/A
c	mM	1.95×10^{-2}	1.70×10^{-1}		2.30
l	cm		37		36
$\mu(\lambda_e)^a$	cm ⁻¹		0.093		0.034
D_0	fs ²	2000	0	0	2100
$\gamma_0(\lambda_f)^a$			0.669		0.630
η_T		0.40	0.43	0.47	0.00058

^a $\lambda_e = 810$ nm, $\lambda_f = 451$ nm

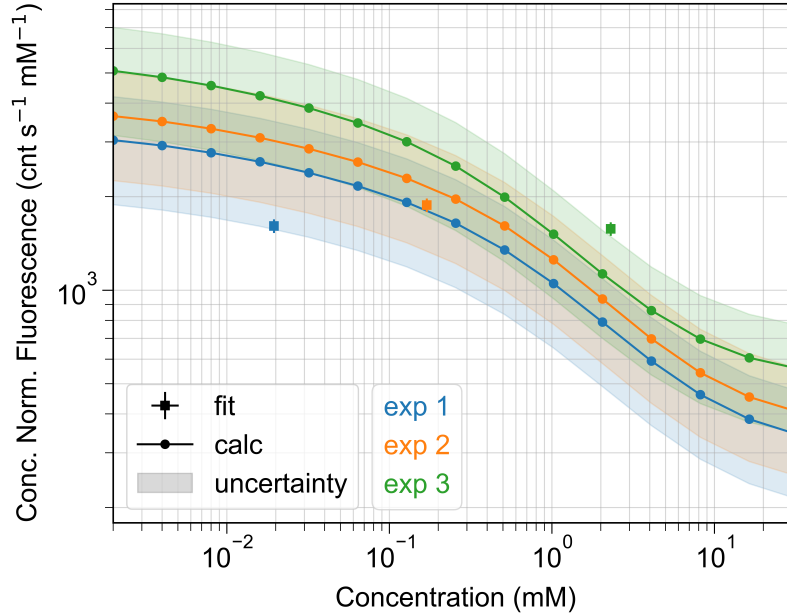


Figure 8: Measured (fit) and calculated (calc) concentration (conc.) normalized (norm.) classical two-photon excited fluorescence at 100 nW excitation as a function of concentration. Experiments 1, 2 and 3 are shown in blue, orange and green respectively. Calculations (using Eq. (18)) were done for each experiment because of minor differences in the setup, which shifts the curve slightly. The calculations predict that as concentration increases there is a general decrease in the concentration normalized fluorescence, which is a result of reabsorption of fluorescence. A shaded region around each of the calculated results show the uncertainty in the calculation. For each experiment, the fit to the measured data was used to extract the concentration normalized fluorescence at 100 nW.

lations and their respective uncertainties.

10 Calculating an E2PA Cross Section Upper Bound

In this section, in a similar manner to Section 9, we discuss the assumptions and equa-

tions used to calculate an E2PEF signal. We arrive at an equation to derive an E2PA cross section upper bound.

We model the E2PEF signal detected on the camera, F_E (cnt s⁻¹), as

$$F_E = g \int_0^l N_E(z) \int_{\lambda_1}^{\lambda_2} \gamma(z, \lambda) \kappa(\lambda) \Phi(\lambda) d\lambda dz, \quad (20)$$

where $N_E(z)$ (excitations cm⁻¹ pulse⁻¹) is the number of excitations per infinitesimal length of fiber dz (cm) per pulse and the other parameters are as mentioned in Section 9. The parameter $N_E(z)$ is defined as

$$\begin{aligned} N_E(z) &= \frac{1}{2} \sigma_E(z) n \mathcal{T} \eta_T(\lambda_e, z) \frac{Q(z)}{g} \\ &= \frac{1}{2} \sigma_E(z) n \mathcal{T} \eta_C \eta_A(\lambda_e, z) \eta_S(\lambda_e, z) \frac{Q(z)}{g}, \end{aligned} \quad (21)$$

where $\sigma_E(z)$ (cm² fluorophore⁻¹) is the E2PA cross section, which has z dependence due to group delay dispersion broadening the entanglement time, \mathcal{T} is the free-space transmission efficiency of the SPDC from the center of the crystal to the fiber, and η_T and η_C are the fiber transmission and coupling efficiencies (Section 6). The other parameters are as mentioned in Section 9.

The parameters \mathcal{T} and η_T are required for E2PA calculations but not for C2PA calculations because E2PA requires that photon pairs stay intact whereas C2PA only requires the presence of single photons. This can be understood by writing the SPDC pair photon rate $Q_{\text{pair}}(z)$ (photon pair s⁻¹) at the fiber as

$$\begin{aligned} Q_{\text{pair}}(z) &= \frac{1}{2} \mathcal{T}^2 \eta_T^2(\lambda_e, z) Q_{\text{xtal}} \\ &= \frac{1}{2} \mathcal{T} \eta_T(\lambda_e, z) Q(z), \end{aligned} \quad (22)$$

where Q_{xtal} (photon s⁻¹) is the (single) photon rate at the crystal and $Q(z)$ is the (single) photon rate at the fiber. More details on this can be found in Ref. 16.

Here we will use the probabilistic model (see for example Ref. 16) to describe $\sigma_E(z)$

(cm² molecule⁻¹) as

$$\sigma_E(z) \approx \frac{\sigma_C}{T_e(z) A_e}, \quad (23)$$

where $T_e(z)$ (fs) is the entanglement time which increases in the presence of group velocity dispersion and thus depends on z and A_e (cm²) is the entanglement area.

We simulate the entanglement time using a discrete Fourier transform of the measured SPDC spectrum shown in Ref. 16. To do this, we estimate the joint spectral amplitude as

$$\begin{aligned} f(\omega_S, \omega_I, z) &= \sqrt{F(\omega_S, \omega_I)} \\ &\times \text{Exp}(i(D_0 + \beta z)(\omega_S - \omega_P/2)^2/2) \\ &\times \text{Exp}(i(D_0 + \beta z)(\omega_I - \omega_P/2)^2/2), \end{aligned} \quad (24)$$

where $F(\omega_S, \omega_I)$ is the measured joint spectral intensity, and ω_S , ω_I and ω_P are the signal, idler and pump frequencies and the parameters D_0 and β are described in Section 9. Discrete Fourier transforms are performed at discrete steps along the fiber of 1 cm and the entanglement time is calculated as the FWHM of projection of the joint temporal intensity along the $(t_S - t_I)$ axis. Here t_S and t_I are the time of arrival of signal and idler respectively. The FWHM is calculated from standard deviation due to the spectrum's non-Gaussian nature. We fit the z -dependence of the resulting T_e values using

$$T_e(z) = 2\sqrt{2\ln 2} \sqrt{T_{e,0}^4 + S_0(\beta z + D_0)^2} / T_{e,0}, \quad (25)$$

where $T_{e,0}$ (fs) and S_0 are fitting parameters and the preceding numerical factors convert standard deviation to FWHM. Physically $T_{e,0}$ should correspond to the entanglement time of the SPDC at the center of the crystal, which is 17 fs, however for our conditions that would render the fit far from ideal. We believe the reason for this is related to the very non-Gaussian form of the spectrum. The parameter S_0 is a numerical factor that is also related to the shape of the spectrum.

In order to estimate a single value for the

E2PA cross section, we will use

$$\sigma_E(0) = \frac{\sigma_C}{T_e(0)A_e}. \quad (26)$$

We can then rewrite Eq. (21) as

$$N_E(z) = \frac{1}{2}\sigma_E(0)n\frac{T_e(0)}{T_e(z)}\mathcal{T}\eta_T(\lambda_e, z)\frac{Q(z)}{g}. \quad (27)$$

Then we can rewrite Eq. (20) as

$$F_E = \frac{1}{2}\sigma_E(0)n\mathcal{T} \int_0^l \frac{T_e(0)}{T_e(z)}\eta_T(\lambda_e, z)Q(z) \\ \times \int_{\lambda_1}^{\lambda_2} \gamma(z, \lambda)\kappa(\lambda)\Phi(\lambda)d\lambda dz. \quad (28)$$

We can solve for $\sigma_E(0)$,

$$\sigma_E(0) = 2F_E \times \left(n\mathcal{T} \int_0^l \frac{T_e(0)}{T_e(z)}\eta_T(\lambda_e, z)Q(z) \\ \times \int_{\lambda_1}^{\lambda_2} \gamma(z, \lambda)\kappa(\lambda)\Phi(\lambda)d\lambda dz \right)^{-1}. \quad (29)$$

Then for a null measurement, we replace F_E by the measurable fluorescence lower bound F^{LB} (cnt s⁻¹) and $\sigma_E(0)$ becomes σ_E^{UB} ,

$$\sigma_E^{\text{UB}} = 2F^{\text{LB}} \times \left(n\mathcal{T} \int_0^l \frac{T_e(0)}{T_e(z)}\eta_T(\lambda_e, z)Q(z) \\ \times \int_{\lambda_1}^{\lambda_2} \gamma(z, \lambda)\kappa(\lambda)\Phi(\lambda)d\lambda dz \right)^{-1}. \quad (30)$$

All the parameters in Eq. (30) are known through experiments or simulations. The parameter F^{LB} is estimated to be 1.0 cnt s⁻¹ based on the signal levels that could be distinguished in these measurements, \mathcal{T} is measured, $T_{e,0}$ and S_0 are estimated using the discrete Fourier transform of the measured joint spectrum, D_0 is estimated, $Q(z)$ is measured, and all other parameters are found as stated in Section 9. The values of these parameters are listed in Tables 2 and 3.

The uncertainty on the derived E2PA cross section upper bound was determined by propagating the errors of the various parameters that go into Eq. (30) and multiplying this value by a coverage factor ($k = 2$), which gives 40%.

References

- (1) Dallas, T.; Dasgupta, P. K. Light at the end of the tunnel: recent analytical applications of liquid-core waveguides. *Trends Anal. Chem* **2004**, *23*, 385–392.
- (2) Khoo, I. C.; Diaz, A.; Ding, J. Nonlinear-absorbing fiber array for large-dynamic-range optical limiting application against intense short laser pulses. *J. Opt. Soc. Am. B* **2004**, *21*, 1234–1240.
- (3) Calcerrada, M.; García-Ruiz, C.; González-Herráez, M. Chemical and biochemical sensing applications of microstructured optical fiber-based systems. *Laser Photonics Rev* **2015**, *9*, 604–627.
- (4) Gerosa, R. M.; Sudirman, A.; de S. Menezes, L.; Margulis, W.; de Matos, C. J. S. All-fiber high repetition rate microfluidic dye laser. *Optica* **2015**, *2*, 186–193.
- (5) Scheibinger, R.; Lüpken, N. M.; Chemnitz, M.; Schaarschmidt, K.; Kobelke, J.; Fallnich, C.; Schmidt, M. A. Higher-order mode supercontinuum generation in dispersion-engineered liquid-core fibers. *Sci. Rep* **2021**, *11*.
- (6) Bhagwat, A. R.; Gaeta, A. L. Nonlinear optics in hollow-core photonic bandgap fibers. *Opt. Express* **2008**, *16*, 5035–5047.
- (7) Chemnitz, M.; Junaid, S.; Schmidt, M. A. Liquid-Core Optical Fibers—A Dynamic Platform for Nonlinear Photonics. *Laser Photonics Rev* **2023**, *17*, 2300126.
- (8) He, G. S.; Bhawalkar, J. D.; Zhao, C. F.; Park, C.-K.; Prasad, P. N. Two-photon-pumped cavity lasing in a dye-solution-filled hollow-fiber system. *Opt. Lett* **1995**, *20*, 2393–2395.
- (9) Khoo, I. C.; Wood, M. V.; Lee, M.; Guenther, B. D. Nonlinear liquid-crystal fiber structures for passive optical limiting of short laser pulses. *Opt. Lett* **1996**, *21*, 1625–1627.

- (10) He, G. S.; Yuan, L.; Bhawalkar, J. D.; Prasad, P. N. Optical limiting, pulse reshaping, and stabilization with a nonlinear absorptive fiber system. *Appl. Opt* **1997**, *36*, 3387–3392.
- (11) Khoo, I. C.; Wood, M. V.; Guenther, B. D.; Shih, M.-Y.; Chen, P. H. Nonlinear absorption and optical limiting of laser pulses in a liquid-cored fiber array. *J. Opt. Soc. Am. B* **1998**, *15*, 1533–1540.
- (12) Williams, G. O. S.; Euser, T. G.; Arlt, J.; Russell, P. S.; Jones, A. C. Taking Two-Photon Excitation to Exceptional Path-Lengths in Photonic Crystal Fiber. *ACS Photonics* **2014**, *1*, 790–793.
- (13) Saha, K.; Venkataraman, V.; Londero, P.; Gaeta, A. L. Enhanced two-photon absorption in a hollow-core photonic-band-gap fiber. *Phys. Rev. A* **2011**, *83*, 033833.
- (14) Hendrickson, S. M.; Lai, M.; Pittman, T.; Franson, J. Observation of Two-Photon Absorption at Low Power Levels Using Tapered Optical Fibers in Rubidium Vapor. *Phys. Rev. Lett* **2010**, *105*, 173602.
- (15) Perrella, C.; Griesser, H. P.; Light, P. S.; Kostecki, R.; Stace, T. M.; Ebendorff-Heidepriem, H.; Monro, T. M.; White, A.; Luiten, A. Demonstration of an Exposed-Core Fiber Platform for Two-Photon Rubidium Spectroscopy. *Phys. Rev. Appl* **2015**, *4*, 014013.
- (16) Parzuchowski, K. M.; Mikhaylov, A.; Mazurek, M. D.; Wilson, R. N.; Lum, D. J.; Gerrits, T.; Charles H. Camp, J.; Stevens, M. J.; Jimenez, R. Setting Bounds on Entangled Two-Photon Absorption Cross Sections in Common Fluorophores. *Phys. Rev. Appl* **2021**, *15*, 044012.
- (17) Rumi, M.; Perry, J. W. Two-photon absorption: an overview of measurements and principles. *Adv. Opt. Photonics* **2010**, *2*, 451–518.
- (18) Javanainen, J.; Gould, P. L. Linear intensity dependence of a two-photon transition rate. *Phys. Rev. A* **1990**, *41*, 5088.
- (19) Gea-Banacloche, J. Two-photon absorption of nonclassical light. *Phys. Rev. Lett* **1989**, *62*, 1603.
- (20) Fei, H.-B.; Jost, B. M.; Popescu, S.; Saleh, B. E. A.; Teich, M. C. Entanglement-Induced Two-Photon Transparency. *Phys. Rev. Lett* **1997**, *78*, 1679.
- (21) Mikhaylov, A.; Parzuchowski, K. M.; Mazurek, M. D.; Lum, D. J.; Gerrits, T.; Camp, C. H.; Stevens, M. J.; Jimenez, R. A comprehensive experimental system for measuring molecular two-photon absorption using an ultrafast entangled photon pair excitation source. *Adv. Opt. Tech. for Quantum Information, Sensing, and Metrology*. 2020.
- (22) Mazurek, M. D.; Parzuchowski, K. M.; Mikhaylov, A.; Nam, S. W.; Camp, C. H.; Gerrits, T.; Jimenez, R.; Stevens, M. J. Bounding Entangled Two-Photon Absorption with Sensitive Transmittance Measurements. *Conf. on Lasers and Electro-Optics*. 2021; p FM3N.2.
- (23) Landes, T.; Allgaier, M.; Merkouche, S.; Smith, B. J.; Marcus, A. H.; Raymer, M. G. Experimental feasibility of molecular two-photon absorption with isolated time-frequency-entangled photon pairs. *Phys. Rev. Res.* **2021**, *3*, 033154.
- (24) Corona-Aquino, S.; Calderón-Losada, O.; Li-Gómez, M. Y.; Cruz-Ramirez, H.; Álvarez Venicio, V.; del Pilar Carreón-Castro, M.; de J. León-Montiel, R.; U'Ren, A. B. Experimental Study of the Validity of Entangled Two-Photon Absorption Measurements in Organic Compounds. *J. Phys. Chem. A* **2022**, *126*, 2185–2195.
- (25) Hickam, B. P.; He, M.; Harper, N.; Szoke, S.; Cushing, S. K. Single-Photon

Scattering Can Account for the Discrepancies among Entangled Two-Photon Measurement Techniques. *J. Phys. Chem. Lett.* **2022**, *13*, 4934–4940.

- (26) Triana-Arango, F.; Ramos-Ortiz, G.; Ramírez-Alarcón, R. Spectral Considerations of Entangled Two-Photon Absorption Effects in Hong–Ou–Mandel Interference Experiments. *J. Phys. Chem. A* **2023**, *127*, 2608–2617.
- (27) Gäbler, T. B.; Hendra, P.; Jain, N.; Gräfe, M. Photon Pair Source based on PPLN-Waveguides for Entangled Two-Photon Absorption. *Adv. Physics Res* **2023**, *3*, 2300037.
- (28) Qian, G.; Liu, X.; Xu, C.; Xu, X.; Wang, D.-W. Experimental test of the entanglement enhancement in two-photon fluorescence. *Quantum Front* **2024**, *3*.
- (29) He, M.; Hickam, B. P.; Harper, N.; Cushing, S. K. Experimental upper bounds for resonance-enhanced entangled two-photon absorption cross section of indocyanine green. *J. Chem. Phys* **2024**, *160*, 094305.
- (30) Landes, T.; Smith, B. J.; Raymer, M. G. Limitations in fluorescence-detected entangled two-photon-absorption experiments: Exploring the low- to high-gain squeezing regimes. *Phys. Rev. A* **2024**, *110*, 033708.
- (31) Tabakaev, D.; Djorović, A.; La Volpe, L.; Gaulier, G.; Ghosh, S.; Bonacina, L.; Wolf, J.-P.; Zbinden, H.; Thew, R. T. Spatial Properties of Entangled Two-Photon Absorption. *Phys. Rev. Lett* **2022**, *129*, 183601.
- (32) Raymer, M. G.; Landes, T.; Marcus, A. H. Entangled two-photon absorption by atoms and molecules: A quantum optics tutorial. *J. Chem. Phys.* **2021**, *155*, 081501.
- (33) Landes, T.; Raymer, M. G.; Allgaier, M.; Merkouche, S.; Smith, B. J.; Marcus, A. H. Quantifying the enhancement of two-photon absorption due to spectral-temporal entanglement. *Opt. Express* **2021**, *29*, 20022–20033.
- (34) Raymer, M. G.; Landes, T. Theory of two-photon absorption with broadband squeezed vacuum. *Phys. Rev. A* **2022**, *106*, 013717.
- (35) Drago, C.; Sipe, J. E. Aspects of two-photon absorption of squeezed light: The continuous-wave limit. *Phys. Rev. A* **2022**, *106*, 023115.
- (36) Moutzouris, K.; Papamichael, M.; Betsis, S. C.; Stavrakas, I.; Hloupis, G.; Triantis, D. Refractive, dispersive and thermo-optic properties of twelve organic solvents in the visible and near-infrared. *Appl. Phys. B* **2013**, *116*, 617–622.
- (37) Malitson, I. H. Interspecimen Comparison of the Refractive Index of Fused Silica. *J. Opt. Soc. Am* **1965**, *55*, 1205–1209.
- (38) Fini, J. M. Microstructure fibres for optical sensing in gases and liquids. *Meas. Sci. Technol.* **2004**, *15*, 1120.
- (39) Kedenburg, S.; Vieweg, M.; Gissibl, T.; Giessen, H. Linear refractive index and absorption measurements of nonlinear optical liquids in the visible and near-infrared spectral region. *Opt. Mater. Express* **2012**, *2*, 1588–1611.
- (40) Frosch, T.; Yan, D.; Popp, J. Ultrasensitive Fiber Enhanced UV Resonance Raman Sensing of Drugs. *Anal. Chem.* **2013**, *85*, 6264–6271.
- (41) Yan, D.; Popp, J.; Pletz, M. W.; Frosch, T. Highly Sensitive Broadband Raman Sensing of Antibiotics in Step-Index Hollow-Core Photonic Crystal Fibers. *ACS Photonics* **2017**, *4*, 138–145.
- (42) Parzuchowski, K. M. Setting Experimental Bounds on Entangled Two-Photon Absorption Cross Sections. PhD thesis, University of Colorado Boulder, Boulder, CO, 2023.

- (43) Kannan, R.; He, G. S.; Lin, T.-C.; Prasad, P. N.; Vaia, R. A.; Tan, L.-S. Toward Highly Active Two-Photon Absorbing Liquids. Synthesis and Characterization of 1,3,5-Triazine-Based Octupolar Molecules. *Chem. Mater* **2004**, *16*, 185–194.
- (44) Rogers, J. E.; Slagle, J. E.; McLean, D. G.; Sutherland, R. L.; Sankaran, B.; Kannan, R.; Tan, L.-S.; Fleitz, P. A. Understanding the One-Photon Photophysical Properties of a Two-Photon Absorbing Chromophore. *J. Phys. Chem. A* **2004**, *108*, 5514–5520.
- (45) de Reguardati, S.; Pahapill, J.; Mikhaylov, A.; Stepanenko, Y.; Rebane, A. High-accuracy reference standards for two-photon absorption in the 680-1050 nm wavelength range. *Opt. Express* **2016**, *24*, 9053–9066.
- (46) Mikhaylov, A.; Wilson, R. N.; Parzuchowski, K. M.; Mazurek, M. D.; Jr., C. H. C.; Stevens, M. J.; Jimenez, R. Hot-Band Absorption Can Mimic Entangled Two-Photon Absorption. *J. Phys. Chem. Lett.* **2022**, *13*, 1489–1493.
- (47) Agrawal, G. P. *Nonlinear Fiber Optics (Sixth Edition)*; Academic Press, 2019; Chapter 2: Pulse propagation in fibers, pp 34–40.